J Geod (2016) 90:1237–1253
DOI 10.1007/s00190-016-0919-4

ORIGINAL ARTICLE

High-frequency Earth rotation variations deduced from altimetry-based ocean tides

Matthias Madzak[1] · Michael Schindelegger[1] · Johannes Böhm[1] · Wolfgang Bosch[2] · Jan Hagedoorn[3]

Received: 23 December 2015 / Accepted: 18 May 2016 / Published online: 15 June 2016

Abstract A model of diurnal and semi-diurnal variations in Earth rotation parameters (ERP) is constructed based on altimetry-measured tidal heights from a multi-mission empirical ocean tide solution. Barotropic currents contributing to relative angular momentum changes are estimated for nine major tides in a global inversion algorithm that solves the two-dimensional momentum equations on a regular 0.5° grid with a heavily weighted continuity constraint. The influence of 19 minor tides is accounted for by linear admittance interpolation of ocean tidal angular momentum, although the assumption of smooth admittance variations with frequency appears to be a doubtful concept for semi-diurnal mass terms in particular. A validation of the newly derived model based on post-fit corrections to polar motion and universal time (ΔUT1) from the analysis of Very Long Baseline Interferometry (VLBI) observations shows a variance reduction for semi-diurnal ΔUT1 residuals that is significant at the 0.05 level with respect to the conventional ERP model. Improvements are also evident for the explicitly modeled K_1, Q_1, and K_2 tides in individual ERP components, but large residuals of more than 15 μas remain at the principal lunar frequencies of O_1 and M_2. We attribute these shortcomings to uncertainties in the inverted relative angular momentum changes and, to a minor extent, to violation of mass conservation in the empirical ocean tide solution. Further dedicated hydrodynamic modeling efforts of these anomalous constituents are required to meet the accuracy standards of modern space geodesy.

Keywords Earth rotation variations · Empirical ocean tides · Tidal currents · Angular momentum changes · VLBI

✉ Matthias Madzak
matthias.madzak@tuwien.ac.at

[1] Department of Geodesy and Geoinformation, TU Wien, Gußhausstraße 27–29, 1040 Vienna, Austria

[2] Deutsches Geodätisches Forschungsinstitut (DGFI-TUM), Arcisstrasse 21, 80333 München, Germany

[3] Technische Universität Berlin, Straße des 17. Juni 135, 10623 Berlin, Germany

1 Introduction

A large fraction of high-frequency Earth rotation variations is due to diurnal and semi-diurnal ocean tides. Water masses are redistributed in response to the tidal forces exerted by the Moon and the Sun, generating relative angular momentum with respect to the rotating reference frame and causing sea surface changes that influence Earth's inertia tensor. These two mechanisms are classically referred to as the motion and mass terms of ocean tidal angular momentum (OTAM, e.g., Chao and Ray 1997) and manifest themselves in perturbations of the Earth's rotation vector. Axial perturbations will affect the rotation rate and may be quantified either as changes in length-of-day (ΔLOD) or increments to universal time (ΔUT1), while equatorial (horizontal) displacements of the rotation axis from the body axis will give rise to polar motion $\{x_p, y_p\}$ and nutation. The subset containing both polar motion and ΔUT1 (or ΔLOD) is commonly referred to as Earth rotation parameters (ERP).

For individual tidal constituents, ocean-induced ERP variations are at the level of a few hundred μas (microarcseconds); cf. Chapter 7 of Petit and Luzum (2010) and note that ΔUT1 is usually reckoned in μs. Early evidence of these signals in geodetic Very Long Baseline Interferometry (VLBI) data by Brosche et al. (1991) and Herring and Dong (1991) was substantiated through refined VLBI and Satellite Laser Ranging (SLR) analyses in the mid-1990s (Sovers et al. 1993; Herring and Dong 1994; Watkins and Eanes 1994; Gipson

1996) and prompted efforts of modeling the tidal effects in an a priori fashion, using hydrodynamic equations and knowledge of the tide-generating potential (Brosche et al. 1989; Seiler 1991; Gross 1993). Exploiting the global record of sea level observations from satellite altimetry, Ray et al. (1994) and Chao et al. (1996) finally documented a satisfactory agreement between space geodetic observations and geophysical model quantities.

At present, the International Earth Rotation and Reference Systems Service (IERS, Petit and Luzum 2010) recommends accounting for the high-frequency ocean tidal ERP variations through routines that build on the "Model C" results of Chao et al. (1996) as derived from Egbert et al. (1994) and Arctic OTAM supplements from Ray et al. (1997)[1]. Several authors have, however, found shortcomings in this model and emphasize the need for an updated version (Steigenberger et al. 2006; Artz et al. 2010; Böhm 2012; Griffiths and Ray 2013). To a minor degree, differences between the observed tidal amplitudes and the values prescribed by the IERS arise from the omission of radiational tidal effects in the coupled atmosphere–ocean system at the order of 5 μas (Brzeziński et al. 2002; Schindelegger 2014) and from slight imperfections (<3 μas Brzeziński 2003) in accounting for the semi-diurnal spin and diurnal polar motion librations of the Earth (Chao et al. 1991). Larger residuals in the range of 15–30 μas are evident for the major gravitational tidal lines (Böhm 2012) and suggest that the analysis of Egbert et al. (1994) was affected by uncertainties in the observed sea level elevations, a comparatively short altimetric dataset, errors in bathymetry charts, or simplified hydrodynamic equations.

One option for revising the current IERS standard is to construct an observation-based ERP model from the tidal variations sensed by VLBI, Global Navigation Satellite Systems (GNSS), or SLR. Several models of this type have been derived in the past and show unprecedented precision levels (Gipson 1996; Steigenberger et al. 2006; Artz et al. 2011). However, such datasets cannot serve as independent standards in the analysis of space geodetic observations and are usually marred by technique-specific systematic errors that leak into the tidal estimates (Griffiths and Ray 2013). In fact, models from different single techniques deviate significantly from each other (Artz et al. 2011). Artz et al. (2012) derived a combined VLBI/Global Positioning System (GPS) model which partly reduces these inconsistencies, but observations from GPS dominate the solution.

A more independent approach is to draw on the increasingly accurate account of ocean tides made possible by altimetry and hydrodynamic modeling; see Stammer et al. (2014) for a recent, comprehensive overview. Three categories of tide models exist and assume different roles in the context of Earth rotation. First, purely hydrodynamic (or forward) tide models are mere solvers of the shallow water equations, using only knowledge of bathymetry and the astronomical forcing. Ideas about drag and dissipation can be tested freely in such environments (Arbic et al. 2004), but—with the exception of the atmosphere driven S_1 tide (Ray and Egbert 2004)—forward-modeled elevations and currents are generally too inaccurate to meet the requirements of space geodesy. Second, assimilation models combine hydrodynamic cores with sea level observations from altimetry in one common adjustment and feature root-mean-square (RMS) misfits of less than 0.6 cm per constituent when validated against ground truth estimates from deep-water bottom pressure stations (Stammer et al. 2014). Accordingly, recent data-assimilative models have been shown to perform well in the analysis of VLBI observations (Böhm 2012). Future developments in that field are thus likely to aid the description of high-frequency signals in Earth rotation. Last, tide models can be also empirical, derived, e.g., from a least-squares harmonic analysis of altimetric measurements without invoking hydrodynamic equations that entail inevitable simplifications. While these models possibly provide the most accurate realization of the true tide in terms of elevation, they do not include any information about the associated deep-water currents which are required for the evaluation of the motion term contribution to OTAM. Yet, using a full elevation grid as constraints, barotropic (2D) currents can be inferred from an inversion of the linearized shallow water equations (Ray 2001).

The main goal of this paper is to deduce and validate an independent model for diurnal and semi-diurnal ERP variations based on EOT11a (EOT for short, Savcenko and Bosch 2012), a state-of-the-art empirical ocean tide model derived at Deutsches Geodätisches Forschungsinstitut from multi-mission satellite altimetry data. Mission-specific weightings are based on a variance component estimate and the residual harmonic analysis up to latitudes of ±81.5° was performed relative to FES2004 (Lyard et al. 2006). In a comparison to ground truth estimates from 151 deep-ocean gauges (Stammer et al. 2014), EOT has been shown to yield reasonably good RMS statistics, similar to those of other contemporary empirical and data-assimilative tide models. A systematically better performance of EOT that would also endorse our model choice in the present work is, it might be admitted, not apparent. We nonetheless emphasize that the network of instruments for the tide determinations in Stammer et al. (2014) is unevenly distributed across the globe and cannot serve as a measure of the broad-scale elevation features that couple to Earth rotation signals (degree-two spherical harmonics). We thus expect EOT to be a reliable source to advance our knowledge of high-frequency ocean tidal ERP variations.

[1] The work of Ray et al. (1994) is often erroneously cited as the source model of the IERS tables; see http://bowie.gsfc.nasa.gov/ggfc/tides/ (accessed 20 March 2016) for a dementi

Having said that, it is also important to set out quantitative measures by which the success of our modeling efforts can be evaluated. Griffiths and Ray (2013) provide evidence that the spurious harmonic aliases seen in nearly all GNSS products are reasonably well simulated if one assumes error amplitudes of 20 % in the conventional ocean tidal ERP model. This estimate of uncertainty is somewhat larger but generally consistent with the spread of ERP tidal corrections from different ocean tide datasets in Böhm (2012). Reducing the present error budget of the IERS model to a level of only a few percent—and thus guaranteeing an accuracy of 1 mm for the deliverables of space geodesy—should serve as an ultimate (though ambitious) goal for studies as the one presented here. Even if these requirements are not adequately met, the method of using and inverting a modern multimission altimetric dataset for the derivation of tidal ERP corrections can point the way forward toward achieving the desired geodetic goals.

We have organized the paper in the following manner. The next section describes the algorithm by which ocean tidal currents are computed from measured elevations, before the treatment of minor tidal effects is discussed in Sect. 3. We validate our ERP model in an analysis of 20-year VLBI observations (Sect. 4) and summarize our results in Sect. 5.

2 Derivation of ocean tidal currents

To derive the flow field from empirical tidal heights, this work uses an inversion method described by Ray (2001). Instead of full hydrodynamic approaches that assimilate altimetry observations into the model, the measured elevations are kept fixed in the estimation procedure, and the currents are inferred from a gradient technique supplemented by a continuity constraint. This approach overcomes several shortcomings of the simple pointwise gradient estimation (Ray 2001), but also transfers the local determination of currents into a global inversion process.

2.1 Dynamic equations

We essentially assume shallow water dynamics with advection and turbulent viscosity terms omitted. The two-dimensional momentum equations in this case are (Ray 2001)

$$\boldsymbol{u}_t + f\boldsymbol{k}\times\boldsymbol{u} + \frac{\boldsymbol{F}}{\rho_w D} = -g\nabla(\zeta - \zeta_{\mathrm{E}} - \zeta_{\mathrm{SAL}}), \tag{1}$$

and the continuity equation reads

$$\zeta_t = -\nabla(D\boldsymbol{u}), \tag{2}$$

with $\boldsymbol{u}_t$ being the time derivative of the horizontal tidal flow $\boldsymbol{u} = (u, v)$ and $f = 2\Omega\sin\varphi$ being the Coriolis parameter, where Ω is the mean angular velocity of the Earth and φ is the geographic latitude. $\boldsymbol{k}$ is a unit vector pointing to the local vertical, ρ_w is the nominal seawater density, D represents the water depth, and g is the gravitational acceleration. ∇ (nabla) is the spherical del operator, denoting horizontal derivatives. The tidal height ζ is reckoned relative to the moving seabed and has to be corrected for equilibrium tidal forcing (ζ_{E}) and self-attraction and loading (ζ_{SAL}), both of which are described below. The stress term $\boldsymbol{F}$ in our linearized model consists of a simple bottom friction of the form (Egbert et al. 1994)

$$\begin{aligned} F_\lambda &= \kappa\rho_w u \\ F_\varphi &= \kappa\rho_w v. \end{aligned} \tag{3}$$

Dissipation schemes accounting for internal wave generation over rough topography (Green and Nycander 2013 2.b and 2.c, *ibid.*) were tested, but resulted in angular momentum deviations of about 10–20 % with respect to established OTAM reference values. In contrast, a uniform frictional parameter led to more satisfactory results that were only weakly dependent on the exact value of κ. Following Ray (2001), we finally adopted $\kappa = 0.01$ ms^{-1} for all of our computations.

Amplitudes (A) and phases (ϕ) of each tidal constituent were converted to complex amplitudes $\hat{\zeta} = A_\zeta e^{-i\phi_\zeta}$, $i \equiv \sqrt{-1}$ and expressed as $\zeta = \hat{\zeta}e^{i\omega t}$, where ω is the tidal frequency. Thus, Eqs. (1) and (2) can be written as (Ray 2001; Logutov and Lermusiaux 2008)

$$i\omega\hat{U} - f\hat{V} + \frac{\kappa\hat{U}}{D} = -\frac{gD}{R_E\cos\varphi}\frac{\partial}{\partial\lambda}(\hat{\zeta} - \hat{\zeta}_{\mathrm{E}} - \hat{\zeta}_{\mathrm{SAL}}) \tag{4}$$

$$i\omega\hat{V} + f\hat{U} + \frac{\kappa\hat{V}}{D} = -\frac{gD}{R_E}\frac{\partial}{\partial\varphi}(\hat{\zeta} - \hat{\zeta}_{\mathrm{E}} - \hat{\zeta}_{\mathrm{SAL}}) \tag{5}$$

$$\frac{1}{R_E\cos\varphi}\left[\frac{\partial\hat{U}}{\partial\lambda} + \frac{\partial(\hat{V}\cos\varphi)}{\partial\varphi}\right] = -i\omega\hat{\zeta}, \tag{6}$$

where $\hat{U} = D\hat{u}$ and $\hat{V} = D\hat{v}$ are barotropic volume transports in the east and north direction, respectively, R_E is the mean radius of the Earth, and (φ,λ) denote latitude and longitude on a sphere. The bathymetry D in our numerical implementation below is a resampled 0.5° version of the 1-min General Bathymetric Chart of the Oceans (GEBCO) data, using moderate Gaussian weighting ($\sigma = 0.5$).

2.2 Equilibrium tide and effects of SAL

Equilibrium tides represent the static response of a hypothetical, frictionless global ocean to differential gravitational forces. Neglecting third- and higher-degree terms, ζ_{E} can be inferred from (Pugh and Woodworth 2014)

$$\zeta_{\mathrm{E}} = \gamma_2 \frac{V_{\mathrm{tid}}}{g}, \tag{7}$$

where V_{tid} is the astronomical tide-generating potential (TGP) and $\gamma_2 = 1 + k_2 - h_2$ is a frequency-dependent modifier to account for the body-tide deformation of the solid Earth using degree-two Love numbers k_2 and h_2 (Hendershott 1972). In Eq. (1), ζ_{E} may be thus conceived as a proxy of the gravitational forcing of each tidal constituent, computed from tabulated equilibrium amplitudes A_{E} for either diurnal (subscript/argument d) or semi-diurnal (subscript/argument s) tides; cf. Table 1 of Arbic et al. (2004):

$$\begin{aligned} \zeta_{\mathrm{E},d}(\varphi, \lambda, t) &= A_{\mathrm{E}}(d)\gamma_2(d)\sin(2\varphi)\cos(\omega(d)t + \lambda) \\ \zeta_{\mathrm{E},s}(\varphi, \lambda, t) &= A_{\mathrm{E}}(s)\gamma_2(s)\cos^2\varphi\cos(\omega(s)t + 2\lambda). \end{aligned} \tag{8}$$

Partial tides not included in Arbic et al. (2004) were taken proportional to the respective potential from the HW95 catalog (Hartmann and Wenzel 1995). An initial ($t = 0$) phase lag for each equilibrium tide was introduced using the fundamental arguments of Simon et al. (1994).

The SAL tide represents a combination of feedback effects on the tidal dynamics that change sea level elevations at the order of 10 % (Accad and Pekeris 1978). On the one hand, the redistributed water masses lead to a yielding of the ocean bottom and the associated body deformations in turn alter the Earth's gravitational field. On the other hand, water is attracted toward the tidal maxima (Gordeev et al. 1977). The rigorous treatment of these effects requires a convolution of the tidal elevation with a proper Green's function (Hendershott 1972), or a computation using spherical harmonics (Pugh and Woodworth 2014). A rough solution can be obtained by introducing a simple scaling factor β, i.e., $\zeta_{\mathrm{SAL}} = \beta\zeta$, with $\beta = 0.085$ usually cited as the optimal choice for the M_2 tide (Accad and Pekeris 1978). Such global values can, however, produce considerable errors, especially in shallow seas (Ray 1998). We therefore calculated the SAL tide from the associated convolution (Ray 1998)

$$\zeta_{\mathrm{SAL}}(\varphi, \lambda) = \rho_w R_E^2 \iint \zeta(\varphi', \lambda')\mathcal{G}(\psi)\cos\varphi' \,\mathrm{d}\varphi' \,\mathrm{d}\lambda', \tag{9}$$

where $\mathcal{G}(\psi)$ are Green's function values computed from a combination of Load Love numbers $\{k'_n, h'_n\}$ (Farrell 1973) and Legendre polynomials depending on the angular distance ψ from the load. We used the tabulated values of $\mathcal{G}(\psi)$ from Stepanov and Hughes (2004), who calculated Green's functions for a bell-distributed mass instead of point masses to overcome the singularity at $\psi = 0$.

2.3 Interlude: OTAM computation

Much of our argumentation below involves OTAM quantities, computed as 2D integrals of tidal heights and volume transports from standard formulae given, e.g., in Chao and Ray (1997) (Eqs. 1 and 2, *ibid.*). Evaluation of the zonal mass term related to the inertia tensor increment ΔI_{33} warrants special consideration, as it is intertwined with the question of mass conservation in global ocean tide models. Following Ray et al. (1997), ΔI_{33} may be broken down into two orthogonal components

$$\Delta I_{33} = -\frac{2}{3}\rho_w R_E^2 \iint_O P_2(\sin\varphi)\,\zeta\,\mathrm{d}O + \frac{2}{3}\rho_w R_E^2 \iint_O \zeta\,\mathrm{d}O, \tag{10}$$

where P_2 is the degree-two Legendre polynomial and O represents the ocean domain with surface element $\mathrm{d}O = R_E^2\cos\varphi\mathrm{d}\varphi\mathrm{d}\lambda$. Tides in the real ocean do conserve mass; hence the total water mass change measured by the second term in Eq. (10) must be identically zero at every instant. In empirical or data-assimilative inverse models of the tides, though, strict mass conversation may be violated when fitting to observational data is prioritized over hydrodynamic information; see Egbert et al. (1994) on how to handle this trade-off in an inverse model. For EOT—as for some other models used in our study—the total water mass change of individual tides is indeed nonzero and perturbs estimates of ΔI_{33} to an uncomfortably large extent, by up to 20 % for the particular case of O_1. This perturbation scales to only a few percent if ΔUT1 changes are evaluated from both inertia effects and the more dominant motion term contribution, but there is no guarantee that a dynamical inconsistency in the global elevation field leaves the associated (and numerically modeled) currents unaffected (Dickman 2010). While corrections of the tidal heights for nonconservation of mass lack clear physical guidelines, a bias in the axial inertia estimate may be avoided if only the first term in Eq. (10) is used to determine ΔI_{33}; see Ray et al. (1997) for further details. This procedure is followed throughout our study and does indeed reduce the spread of zonal mass term estimates from various ocean tide models.

2.4 Inversion algorithm

Equations (4)–(6) together with no-flow constraints at closed boundaries can be written as overdetermined linear system $\boldsymbol{Ax} = \boldsymbol{b}$, where $\boldsymbol{A}$ is a rectangular coefficient matrix, $\boldsymbol{b}$ is the right-hand side vector of observations, and $\boldsymbol{x}$ contains the unknown volume transports derived from a least-squares adjustment. The computations were performed on a staggered grid (C-grid, after Arakawa and Lamb 1977) at a resolution of 0.5° for both input and output data. Hence, the coefficient matrix consists of approximately 500,000 rows and 300,000 columns. The large number of zeros as well as the actual size of $\boldsymbol{A}$ make the use of iterative solvers feasible. Similar to Ray (2001) and Zahel (1995), we adopted the least-

squares algorithm *LSQR* for sparse matrices as published by Paige and Saunders (1982) and provided in MATLAB.

The convergence criterion for the least-squares solver is to compare $\|\boldsymbol{b} - \boldsymbol{Ax}\|/\|\boldsymbol{b}\|$, i.e., the norm of the relative residual in subsequent iterations. The algorithm stops (converges) when it falls below a user-defined tolerance parameter l. To find a reasonable value for l, a calibration experiment was designed based on HAMTIDE11a (HAM for short, Taguchi et al. 2014), an assimilation model for which both tidal elevations and currents are available. Inversions using several tolerances were calculated and converted to OTAM motion terms for comparison to angular momentum estimates from the original HAM flow field. Residuals were found to decrease down to $l = 10^{-9}$ with very little improvement compared to $l = 10^{-8}$. However, for diurnal tides and $l < 10^{-5}$, residuals displayed a somewhat contrasting behavior across the three OTAM components, i.e., an improvement in the z-direction at the expense of increasing OTAM deviations in the y-direction. Hence, a threshold of $l = 10^{-9}$, as used in the calculations presented below, does not guarantee convergence for all constituents. In these cases, the solver was stopped after 200,000 iterations.

A diagonal matrix was used for preconditioning the coefficient matrix, making the $\boldsymbol{L}^2$ norm of all columns equal to one. With this modification, the iterative algorithm converges roughly in half the time. The results were also found to be slightly more accurate when the no-flow boundary conditions were down-weighted by a factor of 0.1. Finally, as discussed by Ray (2001), the continuity equation requires considerably larger weights than the momentum equations to obtain solutions of sufficient accuracy and to overcome singularities at critical latitudes around $\pm 30°$ for diurnal tides and $\pm 75°$ for semi-diurnal tides. Ray (2001) suggests a relative weight of $c = 1000$ for the continuity constraint, which is used as a benchmark value in the following section.

2.5 Comparison with hydrodynamic solutions

A graphical validation of our inversion scheme is presented in Figs. 1 and 2, where volume transports deduced from HAM elevations of the K_1 and M_2 tides are compared to model-intrinsic (U, V) estimates. Global and regional flow patterns agree well among both solutions, but larger differ-

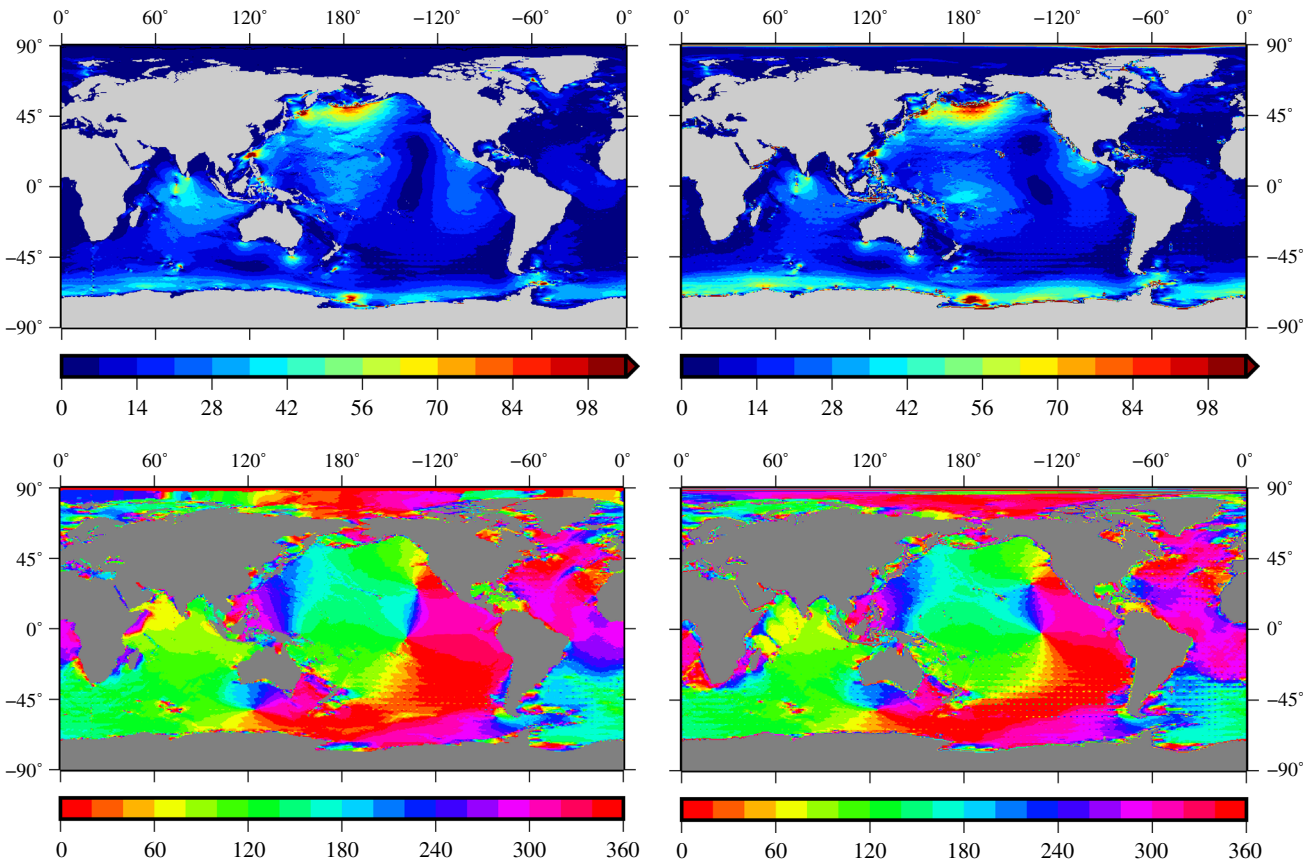

Fig. 1 Results of our tidal current inversion algorithm for K_1. The *right column* displays the estimated volume transports (eastward component U), while the *left column* shows the same component from the hydrodynamic assimilation model HAMTIDE11a. *Upper panels* are amplitudes ($m^2 s^{-1}$), and *lower panels* are phase lags (deg). The spatial resolution is 0.5°, and the weight for the continuity equation is 10,000

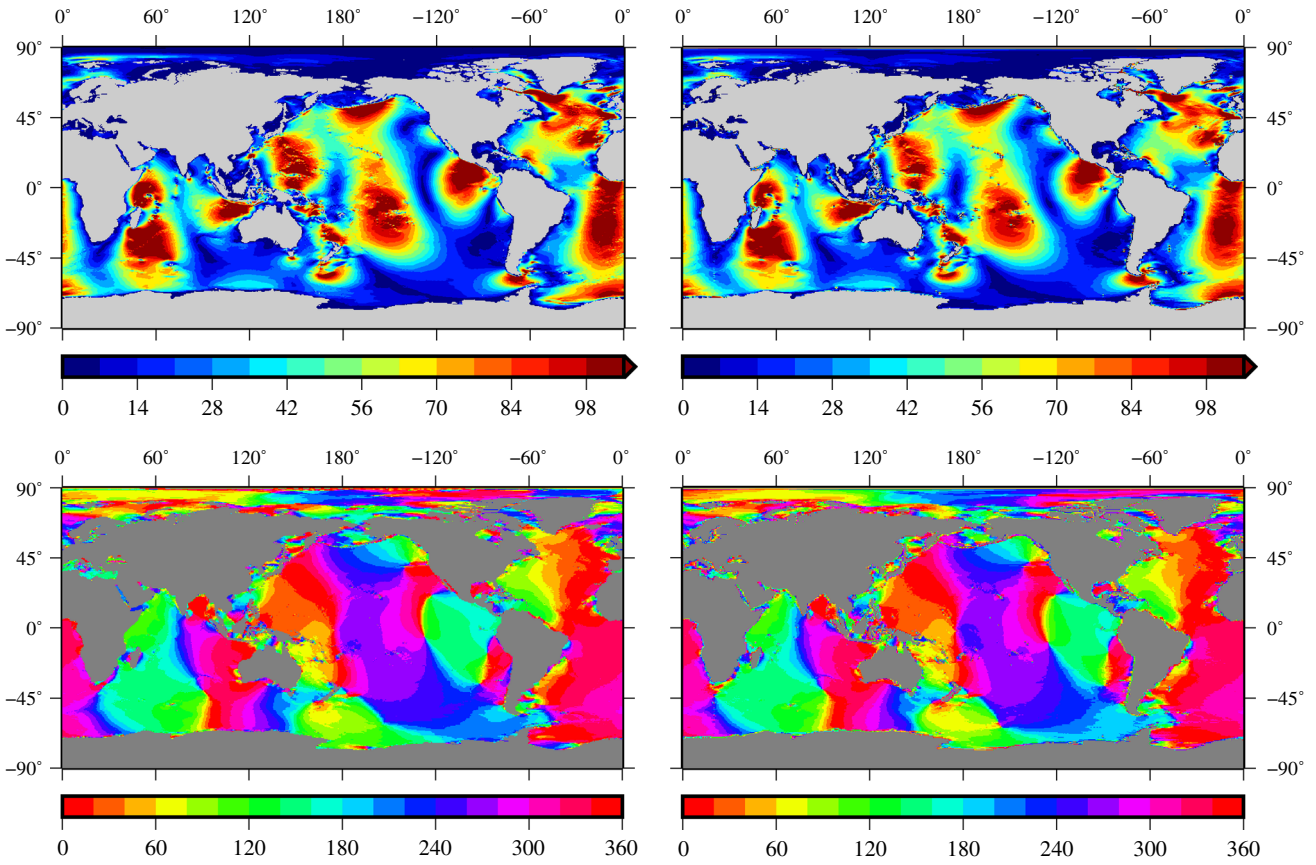

Fig. 2 Same as Fig. 1 but for M_2

ences occur for the diurnal tide K_1. Moreover, pronounced open-ocean peaks arise on a regular grid in Fig. 1 and are particularly evident in the South Pacific and the Atlantic. Phase values in the original HAM data display similar spikes, corroborating Egbert and Bennett (1996)'s observation of sharp unphysical height changes near observational data for which diagonal covariances are assumed in the assimilation procedure. The gradient operator in the momentum equations then acts to magnify the effect in the flow field. We analyzed longitudinal elevation gradients of K_1 from EOT, finding that jittering features in the tidal heights are specifically pronounced in the aforementioned areas. Such small-scale variations might account for the convergence problems of diurnal tides noted in the previous section; yet, they do not necessarily deteriorate our OTAM results, as these estimates are derived from an average-like global integration.

To assess the accuracy of the deduced volume transports and to select proper continuity equation weights, a comparison of EOT-based OTAM values to estimates from the following assimilation models was performed: HAM, FES2012 (Carrère et al. 2012, hereafter FES), and TPXO7.2 (Egbert and Erofeeva 2002 updated version, hereafter TPX). Amplitude-normalized RMS differences for the harmonic variation of each constituent were computed with respect to TPX, ensuring that the tunable parameters of our solver are not systematically biased toward HAM. Figure 3 shows RMS statistics for eight major tides and includes three EOT solutions computed with weights $c = 400$, 1000, and 10,000. Other solutions are omitted for readability reasons.

The comparisons clearly argue against the use of a uniform c value for all tides. Instead, different weights per component and tidal species must be assumed to obtain reasonably accurate OTAM estimates. This result presumably reflects the varying spatial characteristics of the flow field as well as the coupling of equatorial motion terms ($h_{1,2}$) to middle latitudes as against low latitudes in the computation of zonal OTAM estimates h_3. In detail, h_1 and h_2 exhibit the best agreement with TPX using $c = 10{,}000$ for diurnal tides and c between 100 and 400 for semi-diurnal tides. The polar component h_3, by contrast, requires smaller weights for diurnal tides. Differences in relative RMS can reach 50 % or more when adopting $c = 400$ instead of $c = 10{,}000$, which is unacceptable. By and large, the hydrodynamic assimilation models mutually agree within 20 %. To achieve inversion results of equally small deviations from TPX, we implemented varying weights for different tidal

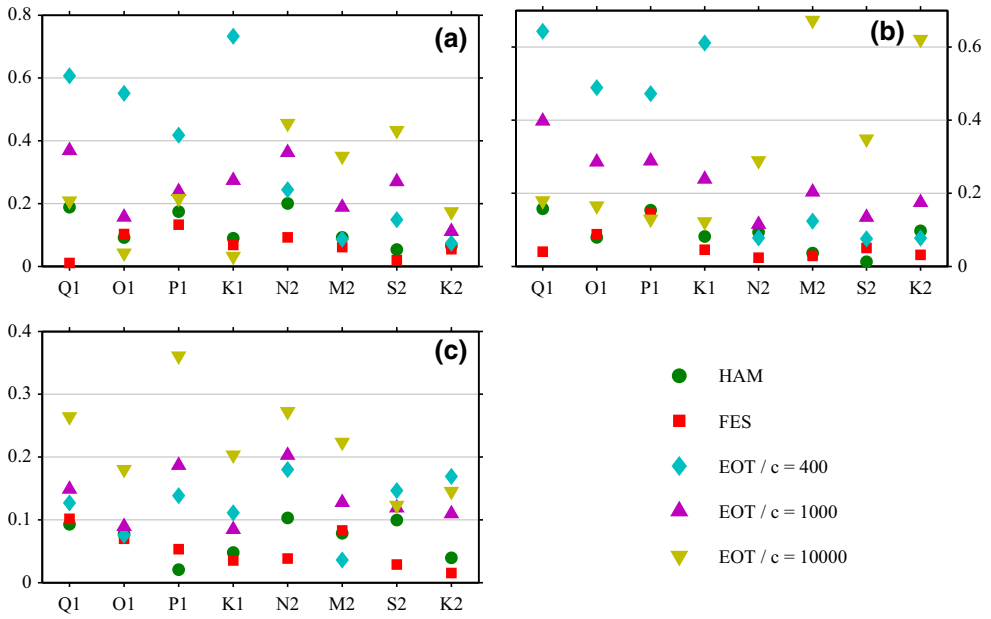

Fig. 3 Relative RMS values (dimensionless) of OTAM motion terms with respect to TPX. Weights for the inversion algorithm for the case of EOT as input are shown in the legend. **a**–**c** denote x, y, and z components

species as well as equatorial and axial components; see Table 1 for the numerical values. The inconsistencies introduced by that approach are accepted in the frame of this study.

An intermediate assessment of the inferred motion terms is presented in tabular and graphical form in the online supporting information. EOT-based relative angular momentum estimates blend in well with results from data-assimilative models (HAM, FES, TPX), even though a moderate underestimation of 10–15 % is apparent for the equatorial components of M_2. Conversely, y motion terms of our K_1 and O_1 inversions are in slight excess of the harmonics from other models. The following sections will disclose whether these discrepancies have any bearing on the accuracy of rotational predictions from EOT.

Table 1 Weights for the continuity equation in the final formulation of the inversion algorithm

Type	Tide	Weight for h_1,h_2	Weight for h_3
Lunar	O_1, Q_1	10,000	100
Solar	P_1	10,000	400
Luni-solar	K_1	10,000	800
Lunar	M_2	200	400
Lunar	N_2	100	200
Lunar	$2N_2$	200	600
Solar	S_2	100	2000
Luni-solar	K_2	200	1000

3 Minor tides and completion of the ERP model

The altimetric tide atlas EOT11a includes nine gravitational tides in the (sub-)diurnal frequency range (Q_1, O_1, P_1, K_1, $2N_2$, N_2, M_2, S_2, K_2), but a larger number of spectral components is required for modern-day ERP models (Gipson 1996; Steigenberger et al. 2006; Artz et al. 2011). One possibility to interpolate these minor tides is the response method as described in Munk and Cartwright (1966). The underlying idea is that the admittance, i.e., the ratio between the tidal height and the associated TGP, is a smooth function of frequency. This assumption is also used by the orthotide formulation (Groves and Reynolds 1975) and validated from an OTAM perspective below.

3.1 Admittance relationships

Given the linearity between tidal elevation and tidal angular momentum, admittance interpolation may be also directly applied on OTAM values. Using global momentum integrals from FES tidal heights and currents, we have assessed the smoothness of this OTAM admittance as a function of frequency. Ratios between x, y, and z OTAM versus TGP are plotted against the tidal period for 12 semi-diurnal and five diurnal constituents in Fig. 4. The TGP was again taken from the HW95 catalog. Evidently, diurnal tides display a flat admittance variation with frequency for both mass and motion terms, but the relationship is much more erratic in the semi-diurnal band. Discontinuities in terms of OTAM partic-

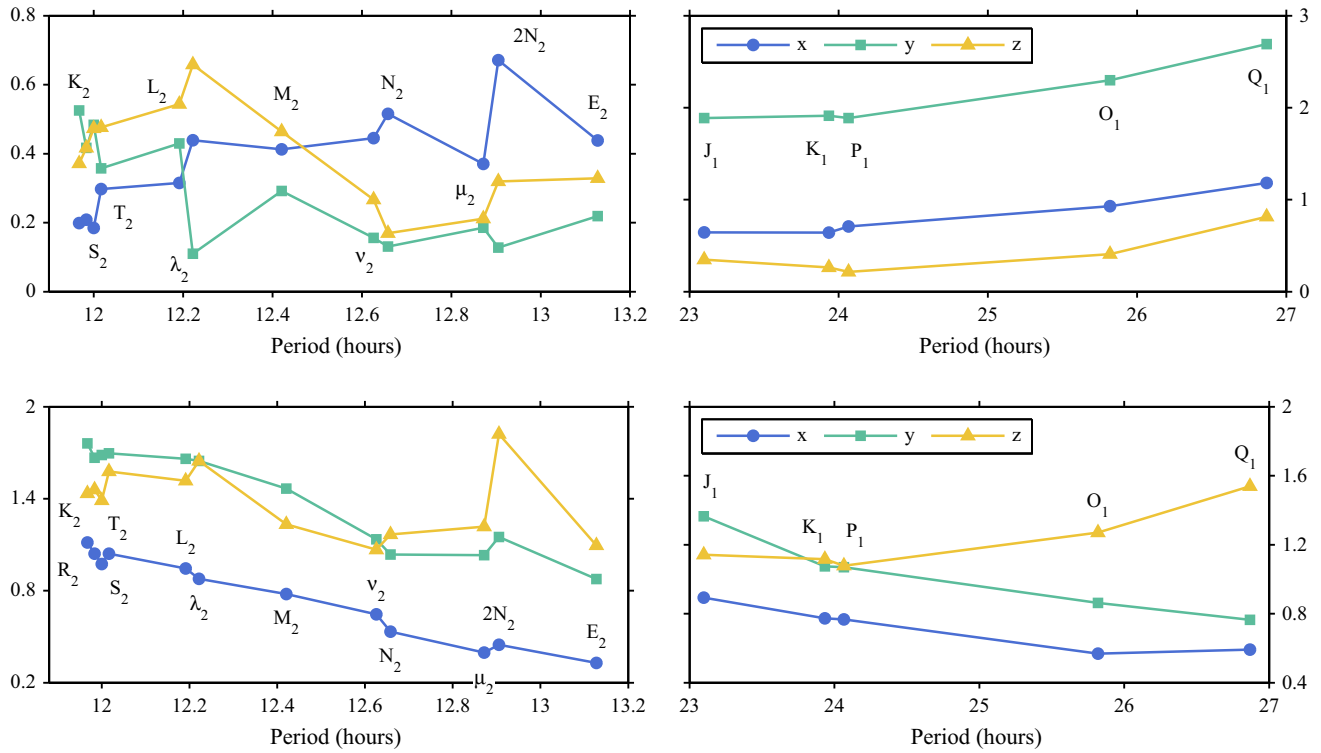

Fig. 4 OTAM interpolation using admittance. Shown are ratio values of OTAM (*upper row*: mass term, *lower row*: motion term) and tidal potential for semi-diurnal (*left*) and diurnal (*right*) tides. Angular momentum values are from FES, and tidal potential amplitudes are from the HW95 catalog. Units: 10^{25} kg m^2/s

ularly arise for the motion component of the $2N_2$ tide. The admittance function of the mass term is even rougher, indicating that the assumption of smoothness for semi-diurnal tides is questionable at least for degree-two spherical harmonics of the elevation field. Yet, in the absence of a physically justified way to overcome this complication, we employed a standard linear interpolation of OTAM values to the minor tidal frequencies of interest. The pivot waves used for the interpolation were taken—if available—in accordance with the IERS Conventions (Table 6.7 in Petit and Luzum 2010); see Madzak (2015) for further details.

A total set of 19 minor tides—down to 1 % of the TGP of M_2—were inferred through admittances to complement the nine major constituents of EOT11a. Selected numerical results for these minor tides are provided in Table 2. In detail, OTAM mass estimates were calculated and compared using two approaches: (1) classically, i.e., through interpolating tidal heights of the ocean tide model EOT and subsequent integration; and (2) alternatively, through a direct interpolation of x, y, and z OTAM between the EOT major tides. The RMS values in Table 2 indicate that the difference between the two approaches is well below 1 % for the majority of minor tidal constituents. In individual cases, the interpolation results can be compared with hydrodynamically modeled solutions from the FES atlas (last column of Table 2). These RMS differences are in the order of 20 % of the OTAM signals, suggesting that input data for minor tides assume a more critical role than the eventual treatment of admittances.

Polar motion and ΔUT1/ΔLOD coefficients for the 28 tidal constituents in our final model were computed using the transfer functions given below and are presented in Tables 5 and 6 in the appendix.

3.2 Excitation formalism

Let $\Delta\hat{I}(\omega)$ be the inertia tensor increment of a particular tide in the frequency domain, and let $\Omega\Delta\hat{I}(\omega)$ be the mass term of OTAM, scaled to the same units as the motion term or relative angular momentum $\hat{h}(\omega)$. In the presence of these perturbations and under the conservation of angular momentum in the solid Earth–ocean system, the linearized Liouville equations for a two-layer Earth dictate the pole position changes $\hat{p}(\omega)$ (Sasao and Wahr 1981; Gross 1993)

$$\begin{aligned}\hat{p}(\omega) = &\left(2.554\times10^{-4}\frac{\Omega}{\omega_{\mathrm{FCN}}-\omega}\right.\\ &\left.+\,2.686\times10^{-3}\frac{\Omega}{\omega_{\mathrm{CW}}-\omega}\right)\frac{\Omega\Delta\hat{I}(\omega)}{A\Omega\tau}\\ &+\left(6.170\times10^{-4}\frac{\Omega}{\omega_{\mathrm{FCN}}-\omega}+1.124\frac{\Omega}{\omega_{\mathrm{CW}}-\omega}\right)\frac{\hat{h}(\omega)}{A\Omega},\end{aligned} \tag{11}$$

Table 2 Comparison of mass terms from (1) admittance interpolation of tidal elevations and (2) admittance interpolation of OTAM for 19 minor constituents

Tide	OTAM[a]	RMS (rel.)	W.r.t. FES
165.565	9.0	7.3 (0.2)	
145.545	11.7	9.3 (0.1)	
275.565	1.8	7.6 (0.5)	
255.545	1.8	7.6 (0.4)	
247.455 (ν_2)	1.3	9.1 (0.7)	245.6 (22.1)
175.455 (J_1)	3.7	3.8 (0.2)	563.8 (20.8)
155.655 (M_1)	4.1	2.6 (0.1)	
237.555 (μ_2)	1.4	22.3 (3.8)	660.7 (70.1)
265.455 (L_2)	1.3	5.7 (0.5)	188.2 (14.4)
272.556 (T_2)	1.3	5.4 (0.5)	463.4 (37.2)
185.555 (OO_1)	2.0	2.7 (0.2)	
137.455 (ρ_1)	2.7	3.4 (0.2)	
135.645	2.8	4.0 (0.2)	
127.555 (σ_1)	2.8	6.8 (0.3)	
155.455	1.5	0.9 (0.1)	
165.545	1.3	1.1 (0.2)	
185.565	1.3	1.7 (0.2)	
162.556 (π_1)	1.3	1.0 (0.2)	
125.755 ($2Q_1$)	2.4	6.1 (0.3)	

Values denote RMS differences of the two approaches, computed as mean over x, y, and z for each tidal line. RMS differences between EOT- and FES-based OTAM estimates are also specified (fourth column). Units: OTAM in column two in 10^{23} kg m^2/s, RMS in 10^{20} kg m^2/s, relative RMS in percent

[a] Computed from interpolated tidal elevations

where $\tau = \Omega^2 R_E^5/(3GA)$, G is the universal gravitational constant, ω_{FCN} and ω_{CW} are the frequencies of the Free Core Nutation (FCN) and the Chandler wobble, respectively, and A designates the principal equatorial moment of inertia. Equation (11) allows for a straightforward extraction of the prograde and retrograde polar motion components for any tidal constituent.

Changes in length-of-day (in seconds per nominal solar day, $\mathrm{LOD}_0 = 86400$ s) relate to the axial mass and motion terms of OTAM $\Omega\Delta I_{33}$ and h_3 through (Gross 1993)

$$\Delta\hat{\mathrm{LOD}}(\omega) = \frac{1}{C_m\Omega}\left(\hat{h}_3(\omega) + 0.756\ \Omega\ \Delta\hat{I}_{33}(\omega)\right), \qquad (12)$$

where C_m is the principal axial moment of inertia of the Earth's crust and mantle. To convert Fourier coefficients of ΔLOD to those of ΔUT1, the following equation can be used:

$$\Delta\hat{\mathrm{UT1}}(\omega) = -i\ (\omega\mathrm{LOD}_0)^{-1}\ \Delta\hat{\mathrm{LOD}}(\omega). \qquad (13)$$

4 Validation using VLBI observations

In this section, we aim to test the quality of our tide-predicted ERP variations within the analysis of nearly 20 years of VLBI observations. We readily admit that such a single-technique validation is not fully rigorous and should be ideally complemented by a reprocessing of long time-span GPS data, which exhibit an arguably greater sensitivity to sub-diurnal terrestrial rotations than VLBI. However, given the ocean modeling character of our study as well as the computational demands of a full GPS analysis, we leave the latter as a potential field of activity for seasoned GNSS analysts. Note also that any GPS-based assessment of tidal ERP signals needs to contend with orbit resonances and associated systematic errors, e.g., for diurnal and near-diurnal polar motion variations (S. Desai, personal communication, 2016).

Along with the short period ERP model derived in the previous section, three other models were used in separate (but identically configured) VLBI solutions. These datasets are (1) FES-based ocean tidal ERP corrections (called VFES); (2) the model recommended by the IERS Conventions 2010 (hereafter IERS); and (3) an empirical standard deduced from GPS and VLBI observations (Artz et al. 2012), subsequently called VIGG. The one based on EOT is denoted by VEOT. Figure 5 shows a priori ERP harmonics for all four datasets and demonstrates that their level of mutual agreement varies depending on the partial tide, as, e.g., P_1 and Q_1 harmonics agree well, but S_2 and M_2 show larger differences throughout. Interestingly, the two models based on current ocean tide knowledge, VFES and VEOT, are occasionally more inconsistent with each other than with any of the remaining datasets; cf., e.g., results for N_2 and S_2 where VEOT closely matches the VIGG values excepting the retrograde band. This and similar findings based on TPX and HAM in Böhm (2012) suggest that even though recent ocean tide models have achieved a good pointwise agreement in terms of elevation, their skill in reflecting the broad-scale (degree-two) features of the tide and the flow field in particular is still far from being satisfactory. The larger uncertainties attached to the motion term contribution are also evident from the spread of OTAM estimates in the online supporting information.

4.1 Input data and processing

Available geodetic VLBI observing sessions were subsetted to a total of 1162 24-h sessions from January 1994 through October 2013 according to some rough measures of the network suitability for the estimation of ERP. These input data include R1 and R4 experiments, i.e., weekly VLBI experiments carried out on Mondays and Thursdays, as well as the continuous VLBI campaigns CONT02, CONT05, CONT08, and CONT11. Hourly values of polar motion and ΔUT1 were obtained in a two-step solution strategy, in which daily

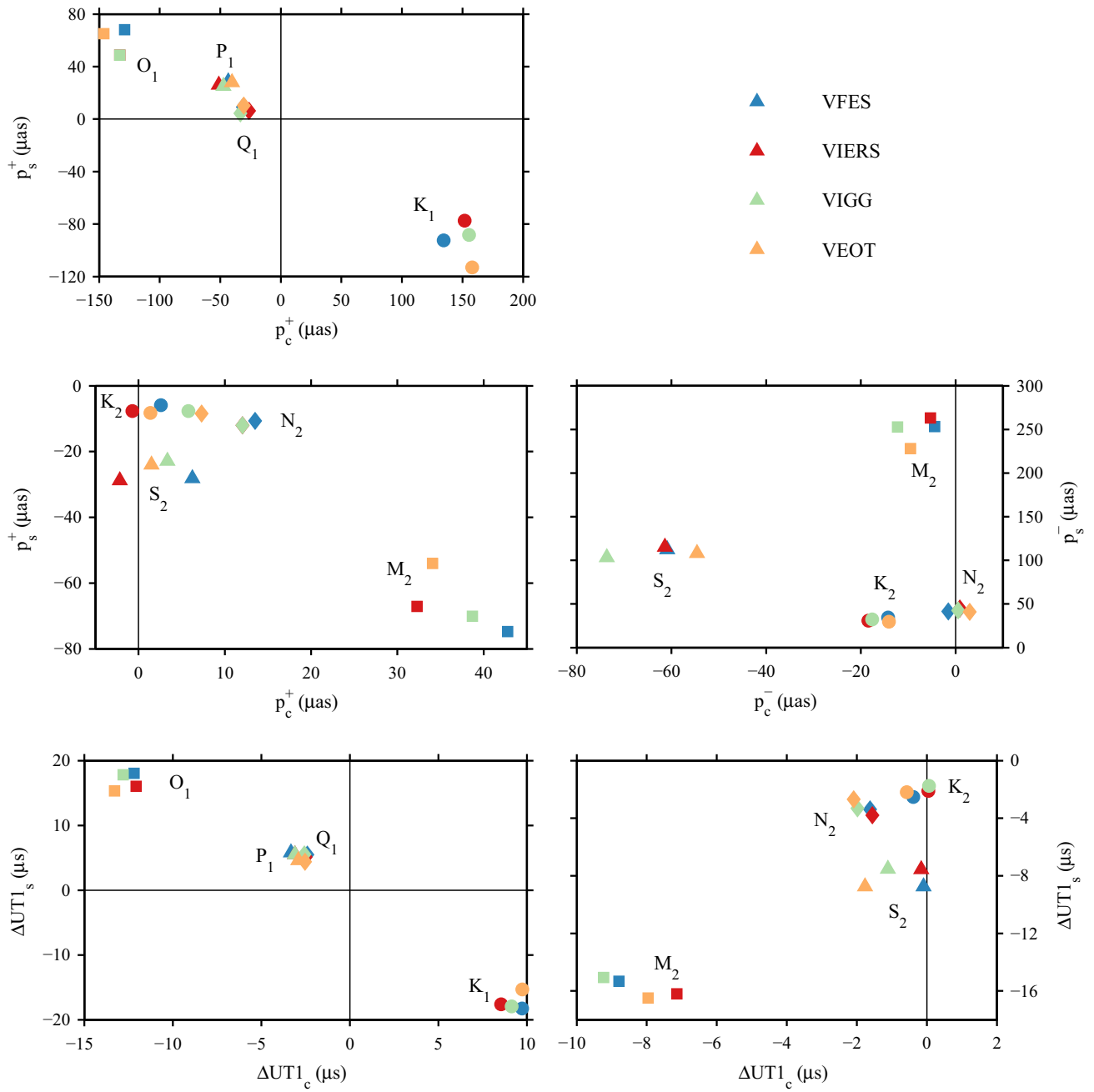

Fig. 5 Phasor diagrams of ERP values for eight major tidal constituents from four input datasets (VFES, IERS, VIGG, VEOT). Subscripts *c* and *s* for polar motion *p* and ΔUT1 denote cosine and sine amplitudes, while '+' and '−' discriminate prograde and retrograde components of *p*; see Petit and Luzum (2010) for the respective phase conventions. Note also the different scalings of *x* and *y* axes in each panel

EOP series were estimated in a first run to derive accurate nutation offsets for all subsequent analyses. Such a standard time series approach allows for an a posteriori fitting of tidal constituents, but neglects possible stochastic relations between rotations and other parameters of the VLBI analysis. A more rigorous method of estimating tidal ERP variations is to express polar motion and ΔUT1 perturbations as sum of sinusoids in the observation equations and solve for the harmonic coefficients simultaneously with other parameters in one global inversion (Gipson 1996). Notwithstanding these conceptual differences, tidal ERP estimates from both approaches have been shown to agree well within the threefold sigma level of any constituent (Böhm 2012).

All processing steps were carried out using the Vienna VLBI Software (Böhm et al. 2012) based on guidelines of the International VLBI Service for Geodesy and Astrometry

Table 3 VLBI analysis configuration for the ERP model validation

Parameter	A priori model	Estimated	Constraint
Ephemerides	JPL421	–	–
CRF	ICRF2	–	–
TRF	VieTRF13 (Krásná et al. 2014)	Offset[a]	NNT/NNR
Polar motion	Pre-solution[b] [IERS 08 C04] + respective high-frequency models (ocean tides, libration)	Hourly [offset[a]]	1 mas after 1 h
ΔUT1	Pre-solution[b] [IERS 08 C04] + respective high-frequency models (ocean tides, libration)	Hourly [offset[a]]	1 ms after 1 h
Prec.-Nut.	Pre-solution[b] [IAU2006/2000A]	– [Offset[a]]	–
Hydrost. delay	Saastamoinen, VMF1	–	–
Wet delay[c]	–	Hourly	1.5 cm after 1 h
Trop. gradients	–	6-Hourly	0.5 mm after 6 h
Clocks[d]	–	Hourly	1.3 cm after 1 h

[a]Per session
[b]In a first step, EOP were determined without estimating high-frequency ERP. Values in square brackets show the a priori source model in this pre-solution
[c]The wet delay was estimated as wet zenith delay
[d]Clocks were estimated as offset + linear trend + quadratic term per clock with respect to a reference clock

Table 4 Comparison of VLBI-derived residuals for the four ERP models used in the present study

	x_p (μas)			y_p (μas)			ΔUT1 (μs)		
Model	RMS (d)	RMS (s)	$\overline{\Delta\varepsilon}$	RMS (d)	RMS (s)	$\overline{\Delta\varepsilon}$	RMS (d)	RMS (s)	$\overline{\Delta\varepsilon}$
VFES	8.5	7.7	−0.52	9.0	9.2	−1.30	0.74	0.80	0.01
IERS	6.9	6.5	1.37	7.8	10.0	−0.70	0.80	0.93	−0.21
VIGG	7.1	7.6	–	6.9	8.6	–	0.60	0.82	–
VEOT	8.3	9.5	0.64	7.2	9.1	−0.07	0.81	0.70	0.06

RMS values for diurnal (d) and semi-diurnal (s) bands were computed from $\sqrt{\overline{A(\varepsilon)^2}/2}$, where A are Fourier coefficient amplitudes of ERP residuals ε and the overbar denotes the arithmetic mean. $\overline{\Delta\varepsilon}$ are median values of Fourier spectrum differences with respect to VIGG

(IVS). Details of our analysis configuration and the treatment of various parameters can be found in Table 3. Note in particular that the IERS prior for spin and polar motion libration in our analysis is sufficiently accurate (∼3 μas for prograde polar motion) to be excluded from the discussion of residuals below; cf. Brzeziński (2003) and references therein. For all three ERP components, the spectral estimates at 47 tidal frequencies were derived within a least-squares adjustment of discrete hourly time series. From the 71 (sub-)diurnal frequencies in the IERS Conventions 2010 (Tables 8.2a and 8.2b), we removed 24 tidal lines that are separated in frequency from other constituents by 1/18 cycle per year or less.

4.2 Discussion of tidal ERP residuals

Fitted tidal residuals ε relative to the background model are small for any suitable high-frequency prior and serve as measure by which the performance of our four ERP models can be compared. Specifically, we have mapped the amplitudes A (ε) for 24 diurnal and 23 semi-diurnal tidal residuals to RMS-like composite statistics and specify the numerical results in Table 4. Being optimized toward space geodetic ERP determinations, VIGG naturally produces lowest RMS scores in an average sense, but the superiority of that model is not as clear-cut as one might suspect. To some extent, the limited sensitivity of VLBI to high-frequency ERP variations conceals the goodness of the GPS-dictated VIGG solution; yet, we note that x_p RMS values from the IERS standard (6.5–6.9 μas) are somewhat below the VIGG differences (7.1–7.6 μas). For ΔUT1 oscillations, diurnal signals appear to be appropriately accounted for by VIGG to a level of 0.60 μs, but ocean tide-predicted ERP models perform exceedingly well for semi-diurnal variations in ΔUT1. The RMS reduction from 0.93 μs for the IERS run to 0.70 μs for VEOT is particularly encouraging and in fact above the 95 % confidence level in a standard t test for 23 semi-diurnal samples.

We now complement and extend the numerical values in Table 4 by analyzing the adjustment results in graphical

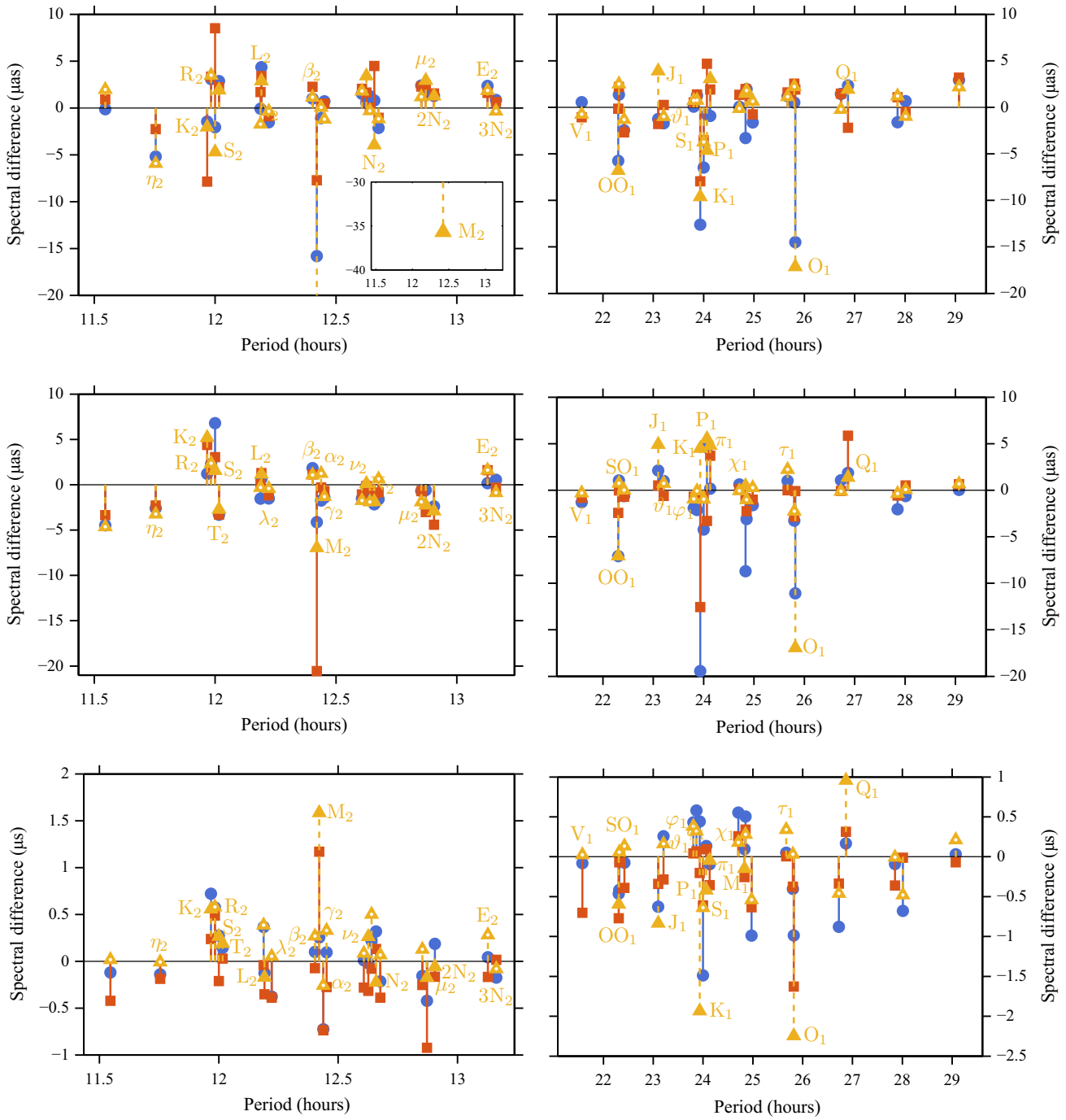

Fig. 6 Differences of amplitude spectra of ERP residuals from VLBI analysis. Smaller values indicate larger ERP residuals compared to the reference (VIGG). *First row*: x_p, *second row*: y_p, *third row*: ΔUT1. VEOT markers filled with a *white circle* indicate that the respective tide is not included in Tables 5 and 6

form. In detail, amplitudes A (ε) from three of the four ERP solutions were subtracted from the fourth—the reference—solution. The larger the residual coefficients of a model, the more negative is the deviation $\Delta\varepsilon$ with respect to the reference. Figure 6 illustrates these differential spectra for both pole coordinates and ΔUT1 in the diurnal and semi-diurnal frequency band. VIGG is taken as reference, so that values below zero imply smaller residuals in the VIGG run. In agreement with Table 4 and the median values of $\Delta\varepsilon$ specified therein, a tendency toward negative spectral differences is indeed observed for y_p variations and the diurnal ΔUT1 component.

VEOT, the model derived from empirical ocean tides, performs well in most aspects, but produces relatively large polar

motion residuals of about −15 μas in the O_1 band as well as a pronounced negative M_2 peak of −35 μas in the direction of x_p. The latter finding is consistent with the moderate underestimation of OTAM motion terms noted in Sect. 2.5. A similar deficiency might have been expected for M_2 in the y_p spectrum, though this particular term appears to be governed by an FCN-amplified mass term that is accurately represented by EOT11a, with an amplitude much smaller than in the IERS source model (3.5×10^{24} kg m^2/s as against 4.3×10^{24} kg m^2/s in Chao et al. 1996). Residuals from the VFES run approach small values for semi-diurnal pole variations, but diurnal tide corrections at O_1 and K_1 in this model deviate from VIGG in the order of 10–20 μas. That polar motion oscillations at K_1 are poorly accounted for by the FES-based tide conforms with the high-latitude regional mass anomalies noted by Stammer et al. (2014) in a comparison of FES to inter-satellite ranging data.

Sizable shortcomings of the IERS model are most obvious in the zonal direction, both for diurnal and semi-diurnal ΔUT1 variations and minor tidal contributions in particular, e.g., at $\nu_1, Oo_1, So_1, J_1, L_2$, or μ_2. For some of these terms, the FES atlas—which models minor tides explicitly—produces a close match with the space geodetic VIGG reference. This result suggests that the handling of minor tidal harmonics in the IERS standard is not without flaws and that modern ocean tide models with a larger number of small constituents can redress such imperfections. Note also that the assumption of zero amplitudes for unconsidered minor tides in the 28-line VEOT model tends to lead to a reduction of residuals relative to VIGG (white dots in Fig. 6).

For our VLBI analysis, VEOT appears to be the most suitable prior model in the semi-diurnal ΔUT1 component, whereas its skill in the diurnal band is affected by errors of the O_1 and K_1 tides. By virtue of the applied admittance interpolation (Sect. 3), these deficiencies are also transferred to many of the surrounding minor tides. At the O_1 line, which has been a notorious anomaly in preceding ERP studies, the relative VEOT residual is −2.3 μs and in considerable excess of $\Delta\varepsilon$ from VFES (−1.0 μs). While the predominant excitation of O_1 tidal variations in Earth's spin comes from the motion component of OTAM, we recall that non-conservation of mass in EOT (and also in FES) is particularly pronounced for O_1; cf. Sect. 2.3. Evidently, the incorporation of global factors such as mass conservation into ocean tide models along with an improved account of the volume transports in low latitudes are pivotal steps toward a credible standard of tide-induced diurnal ΔUT1 variations.

5 Summary and conclusions

The present work has explored one method by which the longstanding necessity for an updated model of sub-diurnal Earth rotation variations due to dynamic ocean tides might be met. Elevation fields of nine major constituents were fixed to a recent empirical ocean tide model, and barotropic volume transports were estimated based on a least-squares inversion of linearized shallow water equations in the fashion of Ray (2001). The recent progress of altimetry-constrained tide models in resolving open-ocean tidal heights to the accuracy of 1 cm (Stammer et al. 2014) prompted high initial expectations for the quality of ERP predictions from this inversion scheme; yet, our study has led to the conclusion that angular momentum changes in the ocean—derived either from the present approach or via data-assimilative forward models—still include uncertainties that make the development of such an ERP model to the 5–10 μas accuracy level difficult. In this respect, the ambitious goal of reducing the ERP model errors by approximately one order of magnitude (cf. Griffiths and Ray 2013) could not be met.

Concerning the modeling approach adopted here, errors of motion terms and hence the numerically deduced tidal currents play a critical role and require knowledge of dissipative terms and the discrete model bathymetry. Comparisons in Madzak (2015) have shown that a simple replacement of the regridded 0.5° GEBCO chart with Shuttle Radar Topography Mission (SRTM) data in an otherwise unchanged least-squares solution alters motion terms in the order of 10 %. Regarding dissipational processes, wave scattering into internal tides near major topographic features is now routinely included in barotropic tide models in parametrized form (Green and Nycander 2013), but no consensus exists about which conversion scheme performs best over a large number of constituents. Employing such drag terms in our linearized momentum equations is straightforward, yet when doing so, one is faced with the task of delimiting them from the bottom friction stresses of the very same linear form.

In addition to unavoidable dynamical approximations, the inversion algorithm used in this study also imposes numerical challenges. Input elevation charts may contain artificial gridding features that affect the convergence of the iterative least-squares solver, while too small frictional parameters in the open ocean generally result in a poorly conditioned coefficient matrix. Above all, the estimated volume transports critically depend on the the relative weight of the continuity constraint against the momentum equations, and credible motion terms were in fact only obtained after having tuned that value per constituent. A dynamically more consistent weighting approach is targeted for future implementations, possibly along with tests of other sparse matrix solvers than the built-in MATLAB algorithm.

By and large, and from the viewpoint of our VLBI validation, the deduced high-frequency ERP model has led to improvements over the current IERS standard for individual major tides (K_1 in y_p, P_1, Q_1, K_2) and several adjacent minor tides accounted for through admittance interpolation. In con-

trast, our results for O_1 and the principal M_2 tide in polar motion are admittedly unsatisfying and require more detailed examination. Full hydrodynamic tide solutions from data-constrained assimilation models appear to be a viable tool to mitigate these problems, and Fig. 6 suggests that advanced fine-resolution tidal atlases such as FES do indeed show signs of convergence with VLBI-derived ERP variations in the semi-diurnal band. Modeling the rotational influences of diurnal tides is still a delicate matter, though, especially for polar motion oscillations that couple to higher latitudes in which altimetric observations are increasingly sparse, the bottom topography is known with limited accuracy, and regional cancellation effects (e.g., due to the Antarctic Kelvin wave) are very pronounced. We are, however, confident that forthcoming altimeter missions and dynamically consistent tide modeling will eventually allow for a precise a priori description of high-frequency Earth rotation variations.

Acknowledgments Open access funding provided by Austrian Science Fund. The authors acknowledge the IVS for providing VLBI observations. Financial support of this study was made available by the Austrian Science Fund (FWF) within projects P24813 and I1479. Efforts from H. Schuh and S. Böhm, who paved the way for this work, are greatly appreciated.

Appendix: Coefficients of the ERP model

Tables 5 and 6 present the diurnal and semi-diurnal polar motion and UT1/LOD variations derived in this study.

Table 5 Ocean tidal variations in polar motion as deduced from EOT. In addition to nine major tides initially included in the altimetric model, OTAM values of 19 minor tides were inferred from linear admittance interpolation

Tide	Delaunay arguments						Doodson number	Period (h)	x_p sin (μas)	x_p cos (μas)	y_p sin (μas)	y_p cos (μas)
	γ	l	l'	F	D	Ω						
SQ_1	1	−2	0	−2	0	−2	125.755	28.0062	0.7	4.8	−4.8	0.7
σ_1	1	0	0	−2	−2	−2	127.555	27.8484	0.9	5.7	−5.7	0.9
	1	−1	0	−2	0	−1	135.645	26.8728	1.9	5.8	−5.8	1.9
Q_1	1	−1	0	−2	0	−2	135.655	26.8684	10.3	30.5	−30.5	10.3
ρ_1	1	1	0	−2	−2	−2	137.455	26.7231	2.0	5.6	−5.6	2.0
	1	0	0	−2	0	−1	145.545	25.8234	12.2	27.4	−27.4	12.2
O_1	1	0	0	−2	0	−2	145.555	25.8193	65.1	146.1	−146.1	65.1
	1	1	0	−2	0	−2	155.455	24.8492	−1.4	−3.8	3.8	−1.4
M_1	1	−1	0	0	0	0	155.655	24.8332	−4.0	−10.5	10.5	−4.0
π_1	1	0	−1	−2	2	−2	162.556	24.1321	1.9	3.3	−3.3	1.9
P_1	1	0	0	−2	2	−2	163.555	24.0659	28.1	40.3	−40.3	28.1
	1	0	0	0	0	1	165.545	23.9380	2.2	3.1	−3.1	2.2
K_1	1	0	0	0	0	0	165.555	23.9345	−113.0	−158.0	158.0	−113.0
	1	0	0	0	0	−1	165.565	23.9310	−15.3	−21.4	21.4	−15.3
J_1	1	1	0	0	0	0	175.455	23.0985	−11.9	−6.4	6.4	−11.9
OO_1	1	0	0	2	0	2	185.555	22.3061	−11.2	−1.9	1.9	−11.2
	1	0	0	2	0	1	185.565	22.3030	−7.2	−1.2	1.2	−7.2
$2N_2$	2	−2	0	−2	0	−2	235.755	12.9054	−6.6	−0.9	1.1	4.0
μ_2	2	0	0	−2	−2	−2	237.555	12.8718	−8.0	−1.1	1.2	4.8
N_2	2	−1	0	−2	0	−2	245.655	12.6583	−49.4	−10.3	4.3	32.5
ν_2	2	1	0	−2	−2	−2	247.455	12.6260	−9.6	−1.8	1.0	6.1
	2	0	0	−2	0	−1	255.545	12.4215	10.6	0.9	−1.6	−6.5
M_2	2	0	0	−2	0	−2	255.555	12.4206	−282.1	−24.6	43.6	174.0
L_2	2	1	0	−2	0	−2	265.455	12.1916	8.4	−1.1	−2.3	−5.3
T_2	2	0	−1	−2	2	−2	272.556	12.0164	−8.2	2.4	3.1	4.7
S_2	2	0	0	−2	2	−2	273.555	12.0000	−132.3	53.1	56.1	84.3
K_2	2	0	0	0	0	0	275.555	11.9672	−38.0	12.7	15.5	21.4
	2	0	0	0	0	−1	275.565	11.9664	−11.4	3.8	4.6	6.3

Table 6 Ocean tidal variations in UT1 and LOD as deduced from EOT. In addition to nine major tides initially included in the altimetric model, OTAM values of 19 minor tides were inferred from linear admittance interpolation

Tide	Delaunay arguments						Doodson number	Period (h)	UT1		LOD	
	γ	l	l'	F	D	Ω			sin (μs)	cos (μs)	sin (μs)	cos (μs)
SQ_1	1	−2	0	−2	0	−2	125.755	28.0062	0.9	−0.3	−1.7	−4.6
σ_1	1	0	0	−2	−2	−2	127.555	27.8484	1.0	−0.4	−2.1	−5.4
	1	−1	0	−2	0	−1	135.645	26.8728	0.8	−0.5	−2.7	−4.7
Q_1	1	−1	0	−2	0	−2	135.655	26.8684	4.4	−2.5	−14.2	−24.6
ρ_1	1	1	0	−2	−2	−2	137.455	26.7231	0.8	−0.5	−2.7	−4.4
	1	0	0	−2	0	−1	145.545	25.8234	2.9	−2.5	−14.5	−16.8
O_1	1	0	0	−2	0	−2	145.555	25.8193	15.3	−13.3	−77.6	−89.5
	1	1	0	−2	0	−2	155.455	24.8492	−0.4	0.3	1.8	2.2
M_1	1	−1	0	0	0	0	155.655	24.8332	−1.0	0.9	5.3	6.3
π_1	1	0	−1	−2	2	−2	162.556	24.1321	0.3	−0.2	−1.4	−1.9
P_1	1	0	0	−2	2	−2	163.555	24.0659	4.6	−2.9	−18.2	−29.0
	1	0	0	0	0	1	165.545	23.9380	0.3	−0.2	−1.3	−1.9
K_1	1	0	0	0	0	0	165.555	23.9345	−15.3	9.7	61.4	96.5
	1	0	0	0	0	−1	165.565	23.9310	−2.1	1.3	8.3	13.1
J_1	1	1	0	0	0	0	175.455	23.0985	−0.7	0.1	0.6	4.3
OO_1	1	0	0	2	0	2	185.555	22.3061	−0.2	−0.3	−1.7	1.7
	1	0	0	2	0	1	185.565	22.3030	−0.2	−0.2	−1.1	1.1
$2N_2$	2	−2	0	−2	0	−2	235.755	12.9054	−0.4	−0.4	−5.0	5.2
μ_2	2	0	0	−2	−2	−2	237.555	12.8718	−0.5	−0.5	−5.9	6.3
N_2	2	−1	0	−2	0	−2	245.655	12.6583	−2.7	−2.1	−24.9	32.1
ν_2	2	1	0	−2	−2	−2	247.455	12.6260	−0.5	−0.4	−4.7	6.4
	2	0	0	−2	0	−1	255.545	12.4215	0.6	0.3	3.5	−7.4
M_2	2	0	0	−2	0	−2	255.555	12.4206	−16.5	−8.0	−96.7	200.3
L_2	2	1	0	−2	0	−2	265.455	12.1916	0.4	0.3	3.1	−4.5
T_2	2	0	−1	−2	2	−2	272.556	12.0164	−0.4	−0.2	−2.1	5.4
S_2	2	0	0	−2	2	−2	273.555	12.0000	−8.7	−1.8	−22.2	109.9
K_2	2	0	0	0	0	0	275.555	11.9672	−2.2	−0.6	−7.2	27.7
	2	0	0	0	0	−1	275.565	11.9664	−0.7	−0.2	−2.2	8.3

References

Accad Y, Pekeris CL (1978) Solution of the tidal equations for the M_2 and S_2 tides in the world oceans from a knowledge of the tidal potential alone. Philos T R Soc A 290:235–266

Arakawa A, Lamb VR (1977) Computational design of the basic dynamical processes of the UCLA general circulation model. MComP 17:173–265

Arbic BK, Garner ST, Hallberg RW, Simmons H (2004) The accuracy of surface elevations in forward global barotropic and baroclinic tide models. Deep-Sea Res PT II 51:3069–3101. doi:10.1016/j.dsr2.2004.09.014

Artz T, Böckmann S, Nothnagel A, Steigenberger P (2010) Subdiurnal variations in the Earth's rotation from continuous Very Long Baseline Interferometry campaigns. J Geophys Res 115(B05404). doi:10.1029/2009JB006834

Artz T, Tesmer née Böckmann S, Nothnagel A (2011) Assessment of periodic sub-diurnal Earth rotation variations at tidal frequencies through transformation of VLBI normal equation systems. J Geodesy 85(9):565–584. doi:10.1007/s00190-011-0457-z

Artz T, Bernhard L, Nothnagel A, Steigenberger P, Tesmer S (2012) Methodology for the combination of sub-daily Earth rotation from GPS and VLBI observations. J Geodesy 86(3):221–239

Böhm J, Böhm S, Nilsson T, Pany A, Plank L, Spicakova H, Teke K, Schuh H (2012) The new Vienna VLBI Software VieVS. In: Kenyon S, Pacino MC, Marti U (eds) Proceedings of IAG Scientific Assembly 2009, vol 136, International Association of Geodesy, pp 1007–1011

Böhm S (2012) Tidal excitation of Earth rotation observed by VLBI and GNSS. In: Geowissenschaftliche Mitteilungen, 90, Department für Geodäsie und Geoinformation, ISSN, pp 1811-8380

Brosche P, Seiler U, Wünsch J, Suendermann J (1989) Periodic changes in Earth's rotation due to oceanic tides. Astron Astrophys 220:318–320

Brosche P, Wünsch J, Campbell J, Schuh H (1991) Ocean tide effects in universal time detected by VLBI. Astron Astrophys 245:676–682

Brzeziński A, Mathews PM (2003) Recent advances in modeling the lunisolar perturbation in polar motion corresponding to high frequency nutation: report on the discussion of the IAU Commission 19 WG on Nutation. In: Capitaine N, Stavinschi M (eds) Proceedings of the Journées systèmes de référence spatio-temporels 2002, pp 101–108

Brzeziński A, Bizouard C, Petrov SD (2002) Influence of the atmosphere on Earth rotation: What new can be learned from the recent atmospheric angular momentum estimates? Surv Geophys 23:33–69. doi:10.1023/A:1014847319391

Carrère L, Lyard F, Cancet M, Guillot A, Roblou L (2012) FES 2012: a new global tidal model taking advantage of nearly 20 years of altimetry. In: Ouwehand L (ed) Proceedings of 20 years of Progress in Radar Altimetry, ESA, Venice, Italy, ISBN 978-92-9221-274-2

Chao B, Dong D, Liu H, Herring T (1991) Libration in the Earth's rotation. Geophys Res Lett 18(11):2007–2010

Chao BF, Ray RD (1997) Oceanic tidal angular momentum and Earth's rotation variations. Prog Oceanogr 40:399–421

Chao BF, Ray RD, Gipson JM, Egbert GD, Ma C (1996) Diurnal/semidiurnal polar motion excited by oceanic tidal angular momentum. J Geophys Res 101(B9):20,151–20,163

Dickman SR (2010) Rotationally acceptable ocean tide models for determining the response of the oceans to atmospheric pressure fluctuations. J Geophys Res 115(B12407). doi:10.1029/2010JB007556

Egbert G, Erofeeva S (2002) Efficient inverse modeling of barotropic ocean tides. J Atmos Oceanic Technol 19(2):183–204

Egbert GD, Bennett AF (1996) Data assimilation methods for ocean tides. In: Malanotte-Rizzoli P (ed) Modern approaches to data assimilation in ocean modeling, Elsevier Oceanography Series, vol 61, Elsevier, pp 147–179

Egbert GD, Bennett AF, Foreman MGG (1994) TOPEX/POSEIDON tides estimated using a global inverse model. J Geophys Res 99(C12):24,821–24,852. doi:10.1029/94JC01894

Farrell WE (1973) Earth tides, ocean tides and tidal loading. Philos T R Soc A 274:253–259

Gipson JM (1996) Very long baseline interferometry determination of neglected tidal terms in high-frequency Earth orientation variation. J Geophys Res 101:28,051–28,064. doi:10.1029/96JB02292

Gordeev RG, Kagan BA, Polyakov EV (1977) The effects of loading and self-attraction on global ocean tides: the model and the results of a numerical experiment. J Phys Oceanogr 7:161–170

Green JAM, Nycander J (2013) A comparison of tidal conversion parameterization for tidal models. J Phys Oceanogr 43:104–119

Griffiths J, Ray JR (2013) Sub-daily alias and draconitic errors in the IGS orbits. GPS Solut 17:413–422. doi:10.1007/s10291-012-0289-1

Gross R (1993) The effect of ocean tides on the Earth's rotation as predicted by the results of an ocean tide model. Geophys Res Lett 20:293–296

Groves GW, Reynolds RW (1975) An orthogonalized convolution method of tide prediction. J Geophys Res 80(30):4131–4138 doi:10.1029/JC080i030p04131

Hartmann T, Wenzel G (1995) The HW95 tidal potential catalogue. Geophys Res Lett 22:3553–3556

Hendershott MC (1972) The effects of solid earth deformation on global ocean tides. Geophys J Int 29:389–402

Herring TA, Dong D (1991) Current and future accuracy of Earth rotation measurements. In: Proceedings of the Chapman conference on Geodetic VLBI: Monitoring Global Change, NOAA technical report NOS 137 NGS, pp 306–324

Herring TA, Dong D (1994) Measurement of diurnal and semidiurnal rotational variations and tidal parameters of Earth. J Geophys Res 99(B9):18,051–18,071

Krásná H, Böhm J, Plank L, Nilsson T, Schuh H (2014) Atmospheric effects on VLBI-derived terrestrial and celestial reference frames. In: Rizos C, Willis P (eds) Earth on the edge: science for a sustainable planet, international association of geodesy symposia, vol 139. Springer, Berlin, pp 203–208

Logutov OG, Lermusiaux PFJ (2008) Inverse barotropic tidal estimation for regional ocean applications. Ocean Model 25:17–34

Lyard F, Lefevre F, Letellier T, Francis O (2006) Modelling the global ocean tides: modern insights from FES2004. Ocean Dyn 56(5–6):394–415. doi:10.1007/s10236-006-0086-x

Madzak M (2015) Short period ocean tidal variations in Earth rotation. Dissertation, Technische Universität Wien

Munk WH, Cartwright DE (1966) Tidal spectroscopy and prediction. Philos T R Soc A 259(1105):533–581

Paige CC, Saunders MA (1982) LSQR: an algorithm for sparse linear equations and sparse least squares. ACM T Math Softw 8:43–71

Petit G, Luzum B (2010) IERS Conventions. IERS Technical Note No. 36, Verlag des Bundesamts für Kartographie und Geodäsie, Frankfurt am Main

Pugh D, Woodworth P (2014) Sea-level science: understanding tides, surges, tsunamis and mean sea-level changes. Cambridge University Press, Cambridge

Ray RD (1998) Ocean self-attraction and loading in numerical tidal models. Mar Geod 21:181–192. doi:10.1080/01490419809388134

Ray RD (2001) Inversion of oceanic tidal currents from measured elevations. J Mar Syst 28(12):1–18. doi:10.1016/S0924-7963(00)00081-6

Ray RD, Egbert GD (2004) The global S_1 tide. J Phys Oceanogr 34:1922–1935

Ray RD, Steinberg DJ, Chao BF, Cartwright DE (1994) Diurnal and semidiurnal variations in the Earth's rotation rate induced by oceanic tides. Science 264:830–832. doi:10.1126/science.264.5160.830

Ray RD, Chao BF, Kowalik Z, Proshutinsky AY (1997) Angular momentum of arctic ocean tides. J Geod 71(6):344–350. doi:10.1007/s001900050102

Sasao T, Wahr JM (1981) An excitation mechanism for the free core nutation. Geophys J R Astron Soc 64(3):729–746. doi:10.1111/j.1365-246X.1981.tb02692.x

Savcenko R, Bosch W (2012) EOT11a—empirical ocean tide model from multi-mission satellite altimetry. Tech. Rep. 89, Deutsches Geodätisches Forschungsinstitut (DGFI), München, Germany

Schindelegger M (2014) Atmosphere-induced short period variations of Earth rotation. In: Geowissenschaftliche Mitteilungen, 96, Department für Geodäsie und Geoinformation, ISSN 1811-8380

Seiler U (1991) Periodic changes of the angular momentum budget due to the tides of the World Ocean. J Geophys Res 96(B6):10,287–10,300. doi:10.1029/91JB00219

Simon JL, Bretagnon P, Chapront J, Chapront-Touze M, Francou G, Laskar J (1994) Numerical expressions for precession formulae and mean elements for the Moon and the planets. Astron Astrophys 282:663–683

Sovers OJ, Jacobs CS, Gross RS (1993) Measuring rapid ocean tidal Earth orientation variations with very long baseline interferometry. J Geophys Res 98(B11):19,959–19,971

Stammer D, Ray RD, Andersen OB et al (2014) Accuracy assessment of global barotropic ocean tide models. Rev Geophys 52:243–282. doi:10.1002/2014RG000450

Steigenberger P, Rothacher M, Dietrich R, Fritsche M, Rülke A, Vey S (2006) Reprocessing of a global GPS network. J Geophys Res 111(B05402). doi:10.1029/2005JB003747

Stepanov VN, Hughes CW (2004) Parameterization of ocean self-attraction and loading in numerical models of the ocean circulation. J Geophys Res 109(C03037). doi:10.1029/2003JC002034

Taguchi E, Stammer D, Zahel W (2014) Inferring deep ocean tidal energy dissipation from the global high-resolution data-

assimilative HAMTIDE model. J Geophys Res-Oceans 119:4573–4592. doi:10.1002/2013JC009766

Watkins MM, Eanes RJ (1994) Diurnal and semidiurnal variations in Earth orientation determined from LAGEOS laser ranging. J Geophys 99(B9):18,073–18,079. doi:10.1029/94JB00805

Zahel W (1995) Assimilating ocean tide determined data into global tidal models. J Mar Syst 6:3–13